Cycling through the glass transition: Evidence for reversibility windows and dynamic anomalies

B. Mantisi,[1] M. Bauchy,[2] and M. Micoulaut[1,*]

[1]*Laboratoire de Physique Théorique de la Matiére Condensée, Université Pierre et Marie Curie, Boite 121, 4 Place Jussieu, 75252 Paris Cedex 05, France*

[2]*Department of Civil and Environmental Engineering, University of California, Los Angeles, Los Angeles, California 90095-1593, USA*

(Received 20 May 2015; published 1 October 2015)

Molecular dynamics simulations of densified glass-forming liquids, $2SiO_2$-Na_2O, are presented. We perform a cooling/heating cycle across the glass transition, and important energy variations are obtained when the material relaxes at low temperature, leading to a hysteresis loop. However, for selected system densities, minuscule energy changes are found, revealing glasses which can be viewed as "thermally reversing," in close correspondence with experiments performed in the context of isostatically rigid glasses. The topological constraint count of the atomic network structure shows that such "reversible" liquids adapt under the density-driven coordination increase, by experiencing larger bond-angle excursions at the atomic scale, quantified from the evolution with density of the Mauro-Gupta function $q(T,\rho)$, which exhibits a broad minimum around $2.75\,\mathrm{g/cm^3}$. The stiffening of the network structure is also evidenced from an inspection of the vibrational density of states, which shows an important decrease in the low-frequency contributions across the reversibility window. Dynamic anomalies are detected from the evolution of isothermal diffusivity with density, which underscore the possible generality of "glass reversibility" in densified tetrahedral glass-forming liquids.

DOI: 10.1103/PhysRevB.92.134201 PACS number(s): 61.43.Fs, 61.25.Em

I. INTRODUCTION

For over a quarter of a century structural aspects of glasses and effects of composition on amorphous networks have been accurately described using rigidity theory [1–3], and this theoretical framework has led to the recognition of a flexible–to–stressed rigid elastic phase transition which was predicted by Phillips [4] and Thorpe [5] using topological constraint enumeration. In this mean-field treatment of rigidity, two broad classes of amorphous networks were identified. Glasses which are weakly connected (e.g., chalcogen-rich such as $Ge_{10}Se_{90}$) are flexible and contain local deformation (floppy) modes which give rise to typical features in the low-frequency part of the vibrational density of states (VDOS) [6], whereas highly connected systems (densified silicas [7], stoichiometric chalcogenides ($GeSe_2$) [8]) are locked by their higher bond density and can be considered to be stressed rigid. The control parameter of the elastic phase transition (such as the temperature in a ferromagnetic transition) has been found to be the network mean coordination number $\bar{r}$, while the order parameter (such as the magnetization in a ferromagnetic transition) turns out to be [9,10] the fraction of floppy modes $f = 3 - n_c$, n_c being the number of constraints per atom arising from nearest-neighbor interactions [4,5]. Since then, experimental validation of rigidity theory has been reported [11–20], and extensions to systems containing broken constraints [21] and to systems containing terminal or dangling ends [22,23] have been proposed. More recently, the incorporation of a temperature dependence has permitted the extension of the approach in a heuristic way [24,25] to glass-forming liquids and to quantitative predictions of properties with composition such as fragility [26], heat capacity jumps [27], hardness [28], and glass transition temperature [29]. Applications of rigidity theory to other complex materials have been reported, such as cement [30] or semiconducting alloys [31].

A decade ago, Boolchand and coworkers established that there exists an intermediate phase (IP) between the flexible ($n_c < 3$) and stressed rigid ($n_c > 3$) elastic phases in such disordered systems [32,33], having a nearly isostatic ($n_c = 3$) character. When properly relaxed at a temperature T/T_g which is independent of composition, the IP boundaries become extremely sharp, and such IPs display a number of remarkable properties, the most notable being their stress-free character [34], resulting in a weak aging dependence in the glassy state [35] of many physical properties; i.e., glasses in the compositional range of the IP do not age much in contrast to glasses outside ($n_c \neq 3$) this compositional range [36]. The stability of the IP is of great importance in a number of areas where appropriate compositions have usually been deduced empirically. The existence of the IP, while being discovered in chalcogenide network glasses, has now also been found in fast-ion-conducting glasses [37,38] and in heavy-metal oxides [39]; these are observations of central interest given that they underscore the general character of isostatic glasses.

Experimentally, the first detection of the IP was obtained from a modulated differential scanning calorimetry (mDSC) measurement [40]. This technique splits the usual DSC signal into a reversing part, which tracks the temperature modulation at the same frequency as the excitation, and a residue, characterized by a nonreversing heat flow, ΔH_{nr}, which contains most of the kinetic events associated with the slowing-down of the relaxation close to the glass transition. This nonreversing heat flow is actually found to nearly vanish in the IP, defining an enthalpic reversibility window (RW), and such observations have been systematically made on a body of nearly 30 different glassy systems. It is highly unfortunate that studies challenging this important discovery in glass science have been overlooking alternative signatures of the IP arising from measurements of the molar volume (a straightforward measurement) [39,41,42], fragility [43,44], Raman mode

*mmi@lptl.jussieu.fr

frequencies [33,34,41–43], and dc conductivity [38]. Another important result that has emerged from the discovery and the characterization of the IP is the recognition that careful sample preparation has to be performed in order to detect the intrinsic elastic behavior revealed from abrupt phase boundaries [41,42]. This has posed the crucial question of the homogeneity [43–45] of the samples under a new and original perspective. In addition, for the special case of oxide glasses, water contamination of the sample has proven to strongly modify the nonreversing heat flow measurement [46].

The endotherm peak that mostly contributes to $\Delta H_{\rm nr}$ over the heating-cooling scan across the glass transition reveals that frozen degrees of freedom during the quench are now excited by temperature, so that the usual enthalpic overshoot at the glass transition is a direct manifestation of the relaxation taking place between room temperature and T_g. The vanishing of $\Delta H_{\rm nr}$ obviously implies that the enthalpic hysteresis loop appearing during the heating/cooling cycle must be minimal given that most of the kinetic events are embedded in this $\Delta H_{\rm nr}$ term.

In the present contribution, using molecular dynamics (MD) simulations we reproduce a typical down- and upscan across the glass transition of a typical densified silicate. It is found that the aforementioned hysteresis loop can be minuscule within a certain density interval, thus allowing us to define a calorimetric RW with density, which is connected to an anomalous behavior in dynamics and a reduction of low-frequency vibrational modes. A connection is made with the softening of bond angles at the molecular level, which adapt under the increasing stress driven by density change. These results provide the first numerical evidence of an RW and make a clear correlation with the notion of network adaptation, a concept which has been introduced in phenomenological models attempting to go beyond the mean-field treatment of rigidity transitions [47–49]. Finally, using reported numerical data on transport properties, we find that the occurrence of diffusivity anomalies (maximum and minimum) are correlated with the boundaries of the RW, thus providing a rigidity viewpoint to waterlike anomalies of densified tetrahedral liquids.

II. SIMULATION DETAILS

The system under investigation (3000 atoms) is a densified sodium silicate liquid ($2SiO_2$-Na_2O, or NS2) that has been investigated from classical MD simulations (integration time using the Verlet algorithm with a 2-fs time step) in (NVT) Ensemble. The atoms interact with a two-body Teter potential [50]. The accuracy of the potential has been demonstrated for structural and dynamic properties [51,52] because calculated diffusion and viscosity are comparable to experimental data [51], and the agreement is substantially improved with respect to alternative potentials [53]. The system has been placed at an equilibration stage at 4000 K over 1 ns (loss of initial configuration) at various densities. Then different cooling procedures (from $q = 100$ K/ps to $q = 0.1$ K/ps) have been performed from 3000 down to 300 K, prior to a heating procedure at the same rate for the 0.1- and 1-K/ps quench. These procedures consist of performing successive incremental steps of simulation time Δt, and the temperature change ΔT between steps is adapted in order to match the desired cooling/heating rate q. Simulations have been performed in NVT Ensemble using a Berendsen thermostat with a relaxation constant of 1 ps $\leqslant \Delta t$. At each step, temperature equilibration could be achieved within a fraction of picoseconds, and the final configuration was used as starting point for the next run at a temperature decreased by ΔT.

In addition, two crystalline disilicate polymorphs have been prepared and simulated under ambient conditions (300 K), i.e., δ-$Na_2Si_2O_5$ (2.41 g/cm^3) and α-$Na_2Si_2O_5$, which is another stable form under ambient condition [54], its structure being made of *zweier* single corner-sharing $SiO_{4/2}$ tetrahedral chains containing Na atoms in between.

III. RESULTS

Figure 1 shows the behavior of the isochoric reduced energy $E^*(T) = E(T,\rho) - 9RT/2$ during cooling for different selected densities ρ. Note that a factor $9RT/2$ is subtracted from the energy, which accounts for harmonic motions in the glassy state. The latter substraction permits us only to highlight the change in slope at the glass transition. For instance, for the highest density ($\rho = 3.50$ g/cm^3), we find from the intercept of the low- and high-temperature behavior of $E^*(T)$ a value for the glass transition temperature of $T_g = 1344$ K.

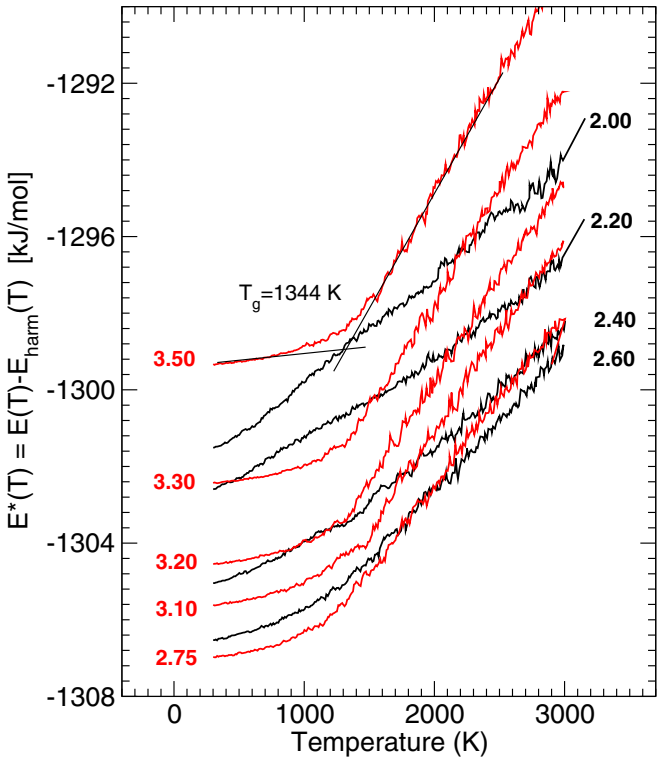

FIG. 1. (Color online) Evolution of the reduced energy $E^*(T) = E(T) - 9RT/2$ of a $2SiO_2$-Na_2O (NS2) liquid during cooling as a function of the temperature for different densities (ranging from 2.00 to 3.50 g/cm^3; black and red curves). Densities are specified close to the curves. The high- and low-temperature extrapolation permits us to define the glass transition temperature (e.g., $T_g = 1344$ K for $\rho = 3.50$ g/cm^3).

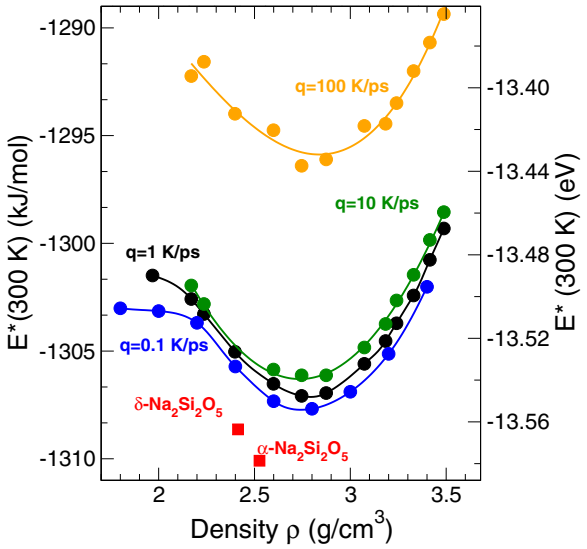

FIG. 2. (Color online) Behavior of the reduced energy $E^*(T,\rho)$ at $T = 300$ K, as a function of the system density ρ for four cooling rates (0.1, 1, 10, and 100 K/ps). The right axis indicates the scale (in eV). The energy E^*(300 K) is also shown [filled (red) squares] for the two stable forms of crystalline $Na_2Si_2O_5$ (α and δ).

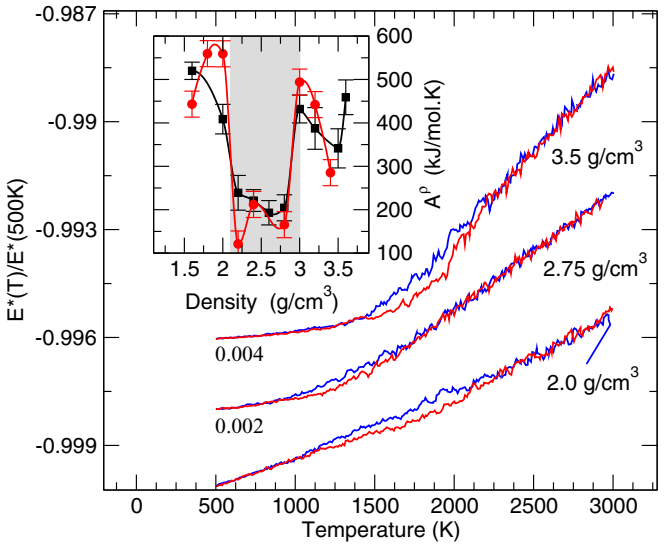

FIG. 3. (Color online) cooling (blue curves) and heating (red curves) cycle ($q = \pm 1$ K/ps) across the glass transition in $2SiO_2$-Na_2O (NS2) liquids for selected densities. Inset: The area (A^ρ) of the energy hysteresis at the glass transition as a function of the system density ρ for 1 K/ps (black curves with squares) and 0.1 K/ps (red curves with circles). The sharp variations of A^ρ leads to the definition of an approximate reversibility window [shaded (gray) zone].

In addition, we note that the total energy of the different densified liquids at low temperature (300 K) is also a function of the system density. $E^*(T,\rho)$ goes through a minimum (Fig. 2) that is obtained for $\rho = 2.75$ g/cm^3, corresponding to an energy of about $\simeq -13.55$ eV for the 1-K/ps quench. A decrease in the density down to 2.00 g/cm^3 leads to a moderate increase in $E^*(T)$, to -13.49 eV, whereas the highest considered density (3.50 g/cm^3) shows a slight increase of about 0.07 eV (compared to 2.75 g/cm^3). This represents about three times the thermal energy k_BT under ambient conditions (0.026 eV). When the glass energy curve is compared to the calculated energy of the α- and δ-disilicate polymorphs, it is seen that for a given density, the energy differences are of the same order as k_BT; i.e., one finds $\Delta E = 0.04$ eV between the δ polymorph and the corresponding glass with the same density (2.40 g/cm^3). The minimum obtained does not depend on the thermal history of the melt given that quench rates that are one (10 K/ps) or two (100 K/ps) orders of magnitude larger lead exactly to the same trend of density and a minimum at around 2.75 g/cm^3. Here, for a fixed density E^*(300 K) increases with the cooling rate, as it should, given that the departure from an equilibrated liquid (e.g., 1344 K for the $\rho = 3.50$ g/cm^3 sample; see Fig. 1) will occur at higher temperatures and higher energies.

Figure 3 now represents a selection of three isochoric cycles for 1 K/ps. Because of the off-equilibrium nature of glasses [55], one usually obtains a hysteretic behavior for the energy driven by the relaxation, and this is, in fact, recovered in the simulation. However, we note that for selected densities (e.g., 2.8 g/cm^3) this hysteresis tends to become very small so that the cooling (blue curve) and the heating (red curve) curves nearly overlap. A way to quantify this observation is to calculate the area A^ρ of the energy change and to follow its behavior as a function of the density (Fig. 3, inset). For fixed densities between $\simeq 2.2$ and 3.0 g/cm^3, a deep square-well minimum in A^ρ is found, indicating that glasses in a particular density range have relaxed in an optimal fashion with minimal changes in energy between the cooling and the heating procedure, i.e., such glasses display a clear tendency to "reversibility," a tendency that is recovered when the cooling/heating rate is changed, i.e., from 1 to 0.1 K/ps. A small minimum is also seen at $\rho \simeq 3.5$ g/cm^3 (for $q = 1$ K/ps) but does not seem to be correlated with the obtained minimum in E^* (Fig. 1).

IV. DISCUSSION

Having obtained these anomalous variations in thermodynamic quantities across the glass transition, we now address the question of their origin from an atomic-scale viewpoint, given that many structural features can be extracted from the MD trajectories.

A. Link with structural properties

The structure of densified silica and silicates is rather well documented [56]. Under ambient conditions the network is made of $SiO_{4/2}$ tetrahedra (the basic unit of silica) that are connected by bridging oxygens (BOs). The addition of an alkali modifier (e.g., Na_2O) leads to the creation of so-called nonbridging oxygens, which have in their close vicinity a sodium cation and which contribute to the depolymerization of the structure [57,58].

We represent in Fig. 4 the calculated fraction of n-fold coordinated silicon species ($n = 4$, 5, 6) along the isotherm 2000 K, which is located in the glass transition and the hysteresis region for all investigated densities (see Fig. 3).

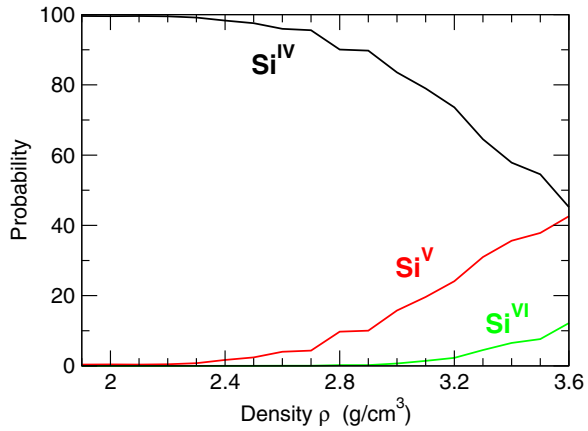

FIG. 4. (Color online) Calculated fraction of n-fold Si species (Si^{IV}, Si^{V}, Si^{VI}) in liquid NS2 (2000 K) as a function of the system density.

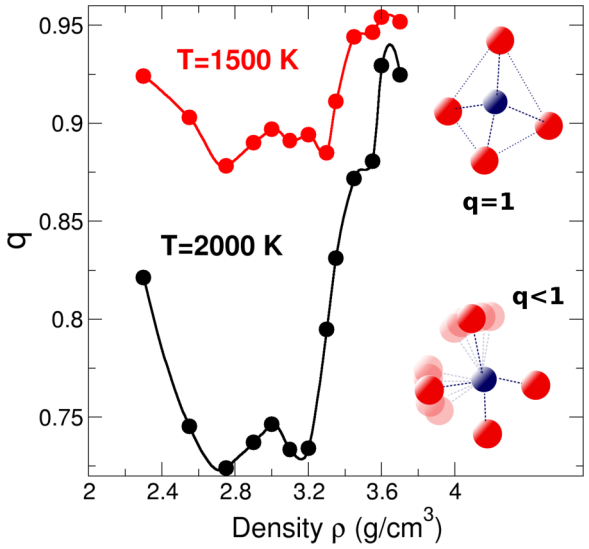

FIG. 5. (Color online) Behavior of the Mauro-Gupta step function $q(T,\rho)$ as a function of the system density along two isotherms belonging to the glass transition domain (1500 and 2000 K). The two possible cases are schematically sketched at the right: either all angular constraints are intact and one has a rigid tetrahedron ($q = 1$) or some of them soften ($q < 1$) in order to adapt under the stress increase produced by the stiffening of the network structure.

The usual behavior of coordination numbers under pressure is recovered [59]; i.e., one obtains the conversion of tetrahedral order ($n = 4$), which prevails under ambient conditions and in low-pressure crystalline polymorphs of silica (e.g., α-quartz), into octahedral order ($n = 6$), which dominates at elevated pressure and in crystalline stishovite [56]. These effects are well described in the literature, from both the experimental [59] and the simulation [60,61] viewpoint, and consistent with these studies we also find an intermediate coordination ($n = 5$) that appears as the the fourfold tetrahedral Si is progressively converted under density increase, the more highly coordinated Si ($n = 6$) growing only for densities higher than 2.8 g/cm^3. An inspection of the trends of the n-fold species with density shows that there are neither abrupt changes nor anomalies that can be correlated with the determined RW (Fig. 3, inset). We therefore conclude that the Si coordination increase alone cannot account for the obtained anomalous thermodynamic behavior during the cooling/heating cycle.

B. Link with network adaptation

The observed trends in thermodynamic variables can actually be correlated with rigidity properties, as discussed next. We analyze such rigidity properties at similar temperatures (1500 and 2000 K) by applying recently introduced methods for computing bond-bending (BB) and bond-stretching (BS) topological constraints from the simulated MD trajectories [62,70–72]. We can, thus, follow such properties for the different densified systems. Given that Si (Fig. 4) and O (not shown; see, e.g., Ref. [73]) coordinations increase with density, corresponding BS constraints increase with density/pressure because $n_c^{BS} = r/2$, where r is the atomic coordination. Note that there is no effect of the sodium cations on rigidity because their associated BS constraints are broken by thermal activation [24,62] at the considered temperature.

We also focus on the BB constraints of BOs defined by two adjacent $SiO_{4/2}$ tetrahedra. For each individual atom k, the angular motion over the time trajectory is recorded, and an atomic bond angle distribution $P_k(\theta)$ characterized by a mean $\langle\theta\rangle_k$ (the first moment of the distribution) and a second moment (or standard deviation σ_k) can be computed. The latter represents a measure of the strength of the underlying BB interaction so that a large (small) σ_k results from a broken (intact) BB constraint [70].

Once system averages are performed (i.e., averages over the number of relevant atoms), one has a distribution $f(\sigma_k)$ of standard deviations, and contributions of low (intact constraints) and large (broken constraints) second moments σ_k to $f(\sigma_k)$ allow estimation of the population $q^{BB}(T,\rho)$ of intact BB constraints. This (step) function $q^{BB}(T,\rho)$ (also termed the Mauro-Gupta function) quantifies the number of BB constraints as a function of the thermodynamic conditions, and one, furthermore, has the obvious limits $q^{BB}(0,\rho) = 1$ (frozen network at $T = 0$) and $q^{BB}(\infty,\rho) = 0$ (all constraints are broken by thermal activation at infinite temperature). According to the approach derived by Mauro and Gupta [24], one has, overall, for a given species i with concentration x, a number of constraints equal to

$$n_c^i(x,T,\rho) = q^{BS}(x,T,\rho)n_c^{BS}(i) + q^{BB}(x,T,\rho)n_c^{BB}(i)$$
$$= q^{BS}(x,T,\rho)r_i/2 + q^{BB}(x,T,\rho)n_c^{BB}(i), \quad (1)$$

where r_i are the coordinations of species Si and O, and $q^{BS}(x,T,\rho)$ and $q^{BB}(x,T,\rho)$ are the step functions which activate bond and angular constraints as the temperature is lowered. Averages over the whole system then lead to the mean number of constraints n_c^{BB}.

Figure 5 shows the calculated evolution of the Mauro-Gupta step function $q^{BB}(T,\rho)$ for the BO BB constraints for two isotherms (1500 and 2000 K), as a function of the system density. Obviously, the number of BB constraints n_c^{BB} of BO atoms also displays an anomalous behavior with density, and a deep minimum in $q^{BB}(T,\rho)$ is found for densities between 2.5 and 3.2 g/cm^3. The network densification leads, indeed, to a

decrease in $q^{\mathrm{BB}}(2000\ \mathrm{K},\rho)$ from $\simeq$0.82 at the glass density (2.40 g/cm^3) to 0.72 at 2.8 g/cm^3, and this minimum in $q^{\mathrm{BB}}(2000\ \mathrm{K},\rho)$ holds up to densities of about 3.2 g/cm^3 at 2000 K. For higher densities, the function $q(T,\rho)$ increases and signals that previously broken angular constraints are now restored. A mild effect of the temperature is also acknowledged because a change from 2000 to 1500 K, while increasing the overall value of $q(T,\rho)$ (thermal activation decreases and constraints are restored), does not dramatically alter the observations and conclusions established for the isotherm 2000 K. The boundaries of the constraint window (2.5 and 3.2 g/cm^3), although somewhat different from the boundaries obtained from the cycle (Fig. 3), obviously connect to these thermal changes at the glass transition.

More generally, Si and O coordination change imposed by densification lead to growth of the network connectivity and the density of stretching interactions (n_c^{BS}). To accommodate this increasing stress and the progressive stiffening of the network structure, the energetically weaker BO interactions (BB) soften and adapt under stress by experiencing larger bond-angle excursions. However, this adaptive situation holds only up to a certain point, given that both Si and O coordination numbers (Fig. 4) will continue to grow with increasing density. The upper limit is obviously detected at 3.2 g/cm^3 for 2000 K, a density at which angles stiffen and $q(T,\rho)$ increases again.

C. Vibrational analysis

We calculate the VDOS $g(\omega)$ using the Fourier transform of the velocity-velocity autocorrelation function,

$$g(\omega) = \frac{1}{Nk_BT}\sum_{j=1}^{N} m_j \int_{-\infty}^{\infty} \langle \mathbf{v}_j(t)\mathbf{v}_j(0)\rangle e^{i\omega t}dt, \qquad (2)$$

where N is either the total number of atoms or the number of atoms of the considered species. Equation (2) can therefore be used separately for the calculation of the total or the partial VDOS using the appropriate mass m_j of the species. Individual spectra for a certain species give information on the vibrations of the considered atoms in the environment more or less constrained by all the other surrounding atoms.

Figure 6 represents the calculated VDOS for the three typical densities corresponding to a low-density, an RW, and a high-density glass. It is shown that the main features of the VDOS (e.g., the 2.00 g/cm^3 system) consist of a broad band between 0 and 110 meV, with an important contribution at $\simeq$20 meV, and a second band made up of a peak at 125 meV together with a secondary peak at 135 meV. These features are typical of silica or silicate-based glasses which contain, indeed, such features at various compositions [63] or densities [64]. A decomposition into species-related contributions (Fig. 6) furthermore reveals that Na atoms contribute mostly at low frequencies ($\omega < 60$ meV), whereas the network-forming species (Si,O) display a broad band between 0 and 110 meV and a secondary band at higher frequencies usually associated with Si-BO-Si bending motions [65].

It is important to emphasize that although the present low-density NS2 glasses can be considered flexible, the VDOS does not contain any vibrational modes with zero frequency (floppy modes) as first suggested by He and Thorpe [9] and

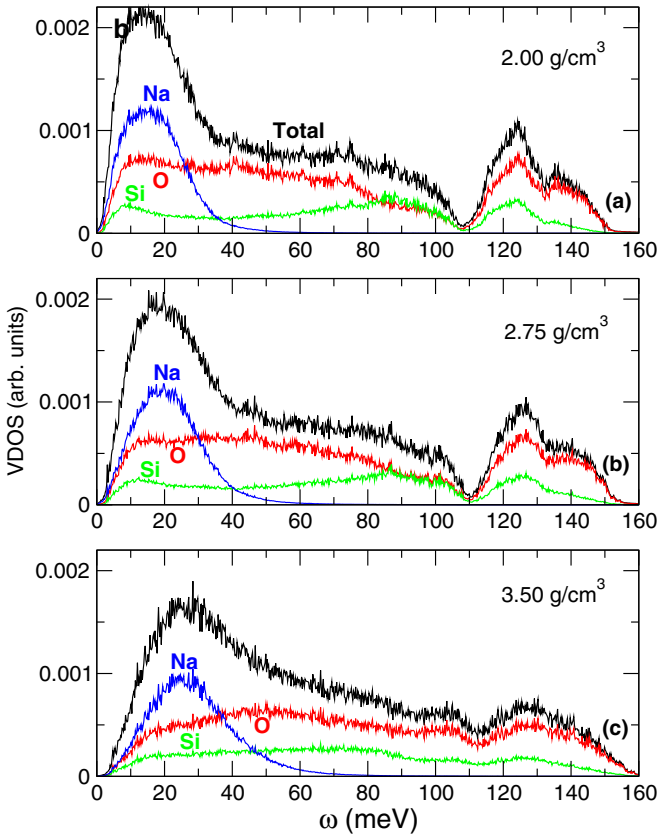

FIG. 6. (Color online) Calculated vibrational density of states (VDOS; black line) for selected densities of the NS2 system at 300 K, and decomposition into partial atomic contributions: (a) ρ = 2.00 g/cm^3; (b) ρ = 2.75 g/cm^3; (c) ρ = 3.50 g/cm^3.

Cai and Thorpe [66] from idealized bond-depleted amorphous networks. These early results contrast with those reported on densified silica networks, where the $SiO_{4/2}$ tetrahedra are considered rigid [67] and which lead to a gap in the VDOS at $\omega \simeq 0$ of stressed rigid glasses. The difference between calculated and experimental spectra has been explained [6] by the fact that residual forces are not taken into account in the initial rigidity approach [9] (dihedral, van der Waals, etc.) and these lead to a finite value for the floppy mode energy of about 5 meV, clearly observed from the experimental VDOS of elemental Se. For the particular case of silica, the contribution of such weak interactions can be estimated to a similar value using the calculated stiffness [68] of the Si-O-Si bending interaction and the molecular mass to form a frequency of 5.8 meV. An alternative and interesting path is provided by the rigid-unit-mode analysis, where the $SiO_{4/2}$ are taken as rigid units [61] and linked by springs, the presence of such rigid unit modes being evidenced by a nonzero value of $g(\omega)$ at $\omega = 0$. The eigenmode analysis of pressure shows that at low ω, $g(\omega)$ decreases with increasing pressure and reaches 0 at about $P \simeq 5$ GPa, at which point $g(\omega) \propto \omega$. Upon further compression, $g(\omega)$ flattens out at the origin, and a rigidity percolation point is identified once $g(\omega) = 0$ at $\omega = 0$.

In order to determine if the low-density region contains floppy modes, following an approach initially introduced by Naumis [69] and recently applied to window glass [70], we

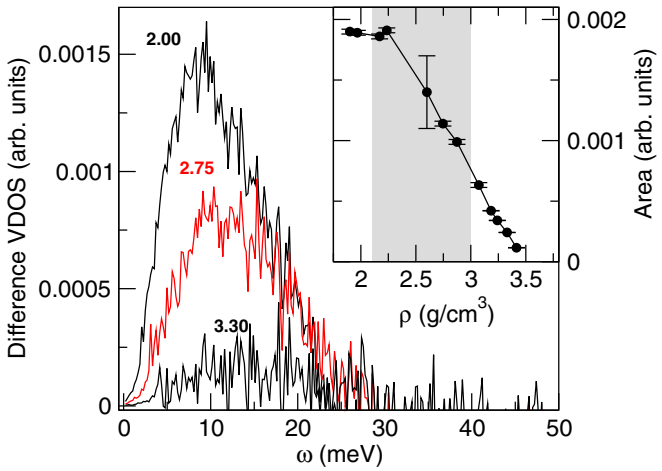

FIG. 7. (Color online) Oxygen difference vibrational density of states (VDOS) plots for selected densities (2.00, 2.75, and 3.30 g/cm^3). Inset: Area of the first peak as a function of system density using a cutoff of 22 meV. The shaded (gray) zone represents the reversibility window in Fig. 3.

decompose the total calculated VDOS into a part arising from low-frequency floppy modes and a part arising from the stressed rigid backbone, i.e., $g(\omega) = g_{\text{floppy}}(\omega) + g_{\text{rigid}}(\omega)$, and focus on the VDOS due only to species that contribute to the stiffness of the network backbone (Si, O). This amounts to representing difference VDOS plots, where a reference VDOS of a stressed rigid glass is taken ($\rho = 3.50$ g/cm^3). The latter choice is arbitrary but since this system is stressed rigid given its large connectedness, this simple substraction allows one to remove low-frequency contributions that are not related to flexibility. Figure 7 shows the low-frequency part of such difference VDOS plots for the oxygen atoms, and an intense peak is detected at around 10 meV. Note that a similar feature is detected for the Si contribution (not shown). This peak frequency is found to be close to the one found for floppy modes in window glasses [70] and is of the same order of magnitude as the one determined experimentally in chalcogenide glasses [6]. One, furthermore, acknowledges an obvious decrease in such low-frequency distributions with increasing density. Building on the analysis in Ref. [6], we determine the floppy mode density by calculating the area A of this prominent peak (Fig. 6, inset). It is found that at a low density, A is nearly constant and does not depend on the density. However, close to the RW boundary, the contribution of this peak to low-frequency vibrations starts to decrease, and an obvious threshold is noted at $\rho \simeq 2.1$–2.2 g/cm^3. A clear relationship among vibrational properties, RWs, and the onset of rigidity is, thus, evidenced.

D. Link with experimental and numerical results

The notion of network adaptation, sometimes also termed "self-organization," is a key feature for understanding the IP in rigidity transitions driven by chemical alloying such as in Ge_xSe_{1-x} glasses [48]. In such systems, the increase in stress is achieved by the addition of Ge cross-links into the flexible network structure [8]. At some point in the compositional space, stress induced by such cross-links can be accommodated during the glass transition, thanks to the accumulation of stress-free subregions that are able to maintain a nearly isostatic character at a local level [34].

Support for this idea has emerged from rigorous approaches using either a vibrational eigenmode analysis of networks constrained by a Keating potential [47], the spin glass cavity method [49], cluster expansions [48], pebble-game algorithms on triangular lattices with equilibration [74], or Bethe [75] or spring networks [76]. MD simulations have led to a structural signature of the IP [77–79], which led to a number of anomalous structural features not necessarily detectable from global experimental functions [80]. The connection between the nonreversing heat flow $\Delta H_{\text{nr}}(x)$, an area which is calculated during the heating/cooling mDSC experiment, and the isostaticity ($n_c = 3$) of glassy networks has been demonstrated theoretically from a simple interaction potential containing both BS and BB interactions [81]. It was found that the enthalpic overshoot in the glass transition endotherm is large in underconstrained ($n_c < 3$) and overconstrained ($n_c > 3$) networks, but it is small in isostatic ($n_c = 3$) networks.

In experimental studies a large number of oxide and chalcogenide glasses exhibit an RW (Fig. 8), which is measured in a similar fashion to our numerical procedure; i.e., the corresponding enthalpic variation is measured from a T_g cycle during an upscan and a downscan using mDSC. Note that, in contrast with the present work, in these experiments rigidity is achieved by a change in composition [42,82], and not by densification. However, an MD study of pressurized silica and germania [67] indeed shows an RW analog with density change that manifests in a temperature-induced densification for selected pressures. Similarly to our findings, changes in the rigidity assuming that network flexibility is only driven by the (oxygen) tetrahedral are found to be directly related to the dynamics of local relaxation events. These are found to be linked to low vibrational properties [7] that are characterized by the vibrational spectra of the rigid unit modes [61].

We mention, among other experimentally investigated systems, Ge-X (X = S, Se [42,82]), Ge-S-I [87], AgPO3-AgI [38], Si-Se [33], SiO_2-Na_2O [58], SiO_2-K_2O [95], Ge-Te-In-Ag [94], Ge-Sb-Se [91], and TeO_2-V_2O_5 [39]. A certain number of comments can be made when all systems are considered at a global level. First, for the simplest systems, i.e., binary network glasses such as Si_xSe_{1-x} and Ge_xS_{1-x}, the boundaries of the RW are found to be all very close, i.e., roughly located between $x = 20\%$ (the isostatic condition, $n_c = 3$) and $x = 25\%$ [Fig. 8(a)]. For such systems, aspects of topology fully control the evolution of the rigidity with increasing group IV atoms because almost no differences can be detected among isovalent systems (Ge-Se, Si-Se, Ge-S).

For the sole lighter chalcogenides, it should be, furthermore, emphasized that a direct relationship can be made with the network mean coordination number $\bar{r}$, given the well-defined coordination numbers which follow the 8-$\mathcal{N}$ rule ($\mathcal{N}$ being the number of s and p electrons). In these cases, the lower boundary of the RW (e.g., $x = 20\%$ Ge in Ge-Se) is found to coincide with the magic value of $\bar{r}_c = 2.4$ corresponding to the mean-field flexible-to-rigid transition [4,5]. For most of the systems, however, discussions based on $\bar{r}$ or the constraint density n_c may be flawed by uncertainties regarding the local structure and the proper definition of the network-forming species

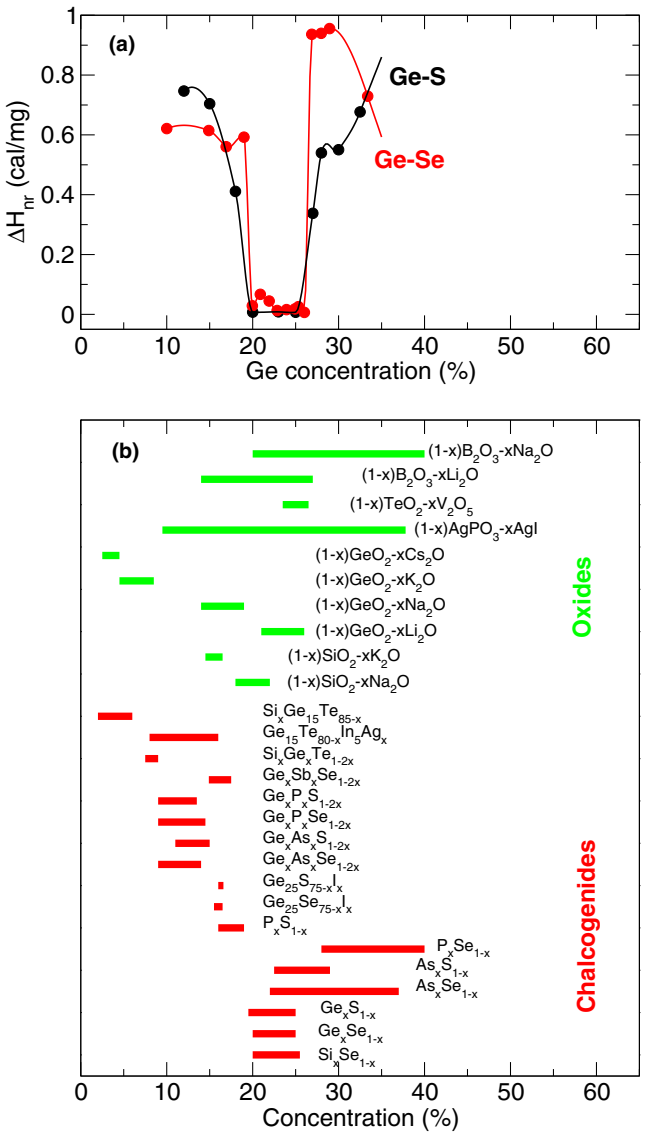

FIG. 8. (Color online) (a) Definition of reversibility windows from calorimetric measurements in Ge-Se [42] and Ge-S [82] glasses, showing a minimum in the nonreversing enthalpy ΔH_{nr}. (b) Location of reversibility windows for different chalcogenide and oxide glass systems: Si-Se [33], Ge-Se [42], Ge-S [82], As-Se [83], As-S [84], P-Se [85], P-S [86], Ge-Se-I [23], Ge-S-I [87], Ge-As-Se [88], Ge-As-S [89], Ge-P-Se [35], Ge-P-S [90], Ge-Sb-Se [91], Si-Ge-Te [92,93], Ge-Te-In-Ag [94], SiO_2-M_2O (M = Na, K) [58], GeO_2-M_2O (M = Li, K, Cs) [95], GeO_2-Na_2O [96], $AgPO_3$-AgI [38], TeO_2-V_2O_5 [39], and B_2O_3-M_2O (M = Li, Na) [97].

contributing to rigidity. As a result, coordination numbers and related active/inactive constraints can only be guessed and must be derived from specific structural models, as detected when group V selenides/sulfides are being considered. This family of systems exhibits, indeed, different locations for the RW compositions, e.g., differences emerge between sulfides and selenides and between As- and P-bearing chalcogenides. Local structural features have been put forward to explain the trends and the differences [84–86] as well as the special effect of sulfur segregation in sulfide-rich glasses [84,86,89], and these have also served for the characterization of related ternaries [89–90]. The validity of such structural models is still debated in the literature.

Our general statements and observations remain valid when the tellurides are considered. Because of the increased electronic delocalization of the Te atoms, groups IV and V atoms do not necessarily follow the 8-$\mathcal{N}$ rule and lead to mixed local geometries that are now composition dependent, e.g., sp^3-tetrahedral and defect-octahedral for Ge atoms, so that a rigourous constraint count must rely on accurate *ab initio* simulations, in conjunction with MD-based constraint counting algorithms [62,70–72]. These conclusions can be maintained to some extent for the wide class of oxides (Fig. 8) which display the same phenomenology as the chalcogenide networks; i.e., an RW is found between the two end limits of possible networks or elastic phases. These are either highly connected and stressed rigid (e.g., silica) or strongly depolymerized and flexible (e.g., lithium pyrosilicates, SiO_2-$2Li_2O$). In such binary systems, alkali cation size effects have, furthermore, been discovered, as exemplified in silicates and germanates, the increase in cation size leading to a shift of the RW to a lower alkali content. Phenomenological models based on additional broken constraints have been reported [58,98], and some MD simulations have also been proposed [99] to better understand such interesting trends at the atomic level.

Finally, we note that a certain number of well-known anomalies of binary oxides (the "germanate anomalies" [96,100], the "borate anomaly" [97]) seem to be correlated with the RW, given that compositions at which such anomalies take place actually coincide with those of the RW. For the particular example of sodium germanates, the reported density anomaly [100], showing a minimum in molar volume around 16% Na_2O, is simply a manifestation of the space-filling tendency that results from the adaptive isostatic nature of RW compositions [96]. A similar conclusion can be drawn for borates [97].

The observation of an RW thus appears to be generic because the same observations have been made on a variety of glass systems, simple chalcogenides, ternary compounds, binary oxide glasses, chalcohalides, heavy-metal oxides, etc. These observations are, clearly, system dependent, but salient features are clearly visible when the same family of compounds is investigated. Their behavior bears striking similarities to the present obtained MD RWs.

E. Link with diffusivity and the waterlike anomaly

The simulated NS2 liquid also exhibits a series of dynamic anomalies that manifest by diffusivity maxima and minima [51,101] [Fig. 9(a)] and also by viscosity minima [51]. In addition, when both diffusivity and viscosity are studied as a function of temperature in an Arrhenius plot, it has been found that the corresponding activation energies for viscosity or diffusion also display a minimum for the same range of pressures/densities in which the diffusivity exhibits these anomalies [101]. This indicates the increased ease of relaxation in adaptive network-forming liquids that ultimately contributes to the nearly reversing character of the glass transition (Fig. 3).

The obtained diffusivity anomaly for the present NS2 liquid (Fig. 9) also relates to transport anomalies reported for densified tetrahedral liquids [103,104] as illustrated by the

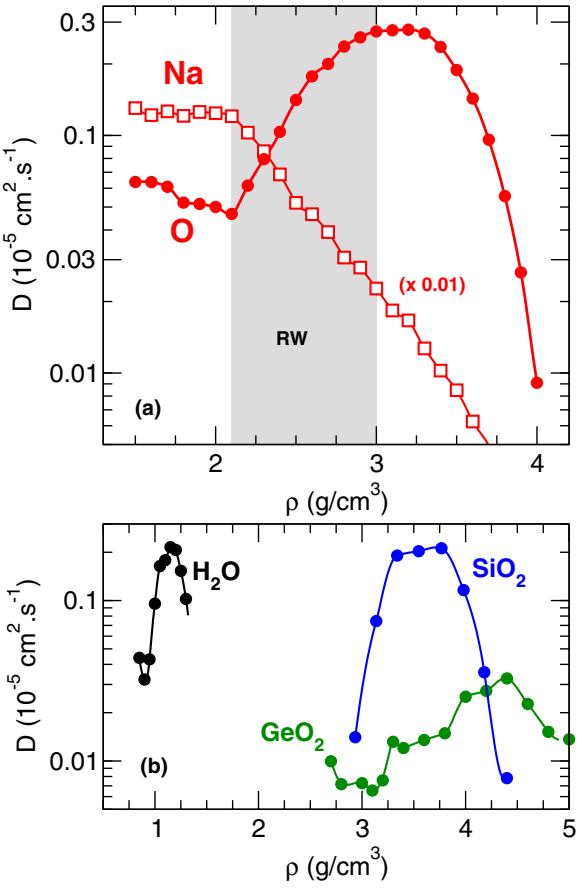

FIG. 9. (Color online) (a) Oxygen and sodium diffusivities [102] in liquid NS2 (2000 K) as a function of the system density, compared to the location of the reversibility window (RW) (minimum of the hysteresis area of the energy determined from Fig. 3). (b) Oxygen diffusivity in densified tetrahedral liquids as a function of the system density: liquid water (black curve; 220 K [104]), silica (blue curve; 2500 K [103]), and germania (green curve; 1200 K [105]). Note that a minimum in D for silica appears only at higher temperatures.

well-known example of densified water [104]. The correlation becomes obvious when we represent the oxygen diffusivity D_O of NS2 as a function of the system density [100] and compare [Fig. 9(b)] the trend with corresponding results for densified silica (2500 K [103]), water (220 K [104]), or germania (1200 K [105]).

In studies on structural and dynamic anomalies of densified tetrahedral liquids, it has been stressed [103,104] that the definition of local structural order parameters [106] could help in understanding the relationships between such diffusivity anomalies and structural and thermodynamic anomalies under temperature and density change. One order parameter (translational) measures the tendency of pairs of molecules to be separated by a preferential distance, while a second order parameter (orientational) measures the tendency of a molecule and its nearest neighbors to adopt preferential orientations.

Using our results, one now recognizes that the diffusivity anomalies of liquid NS2 connects to the RW (Fig. 9), driven by constraint softening, which is the dominant feature controlling the evolution of the transport coefficient under density and temperature change. We, thus, view these transport anomalies as a consequence of structural rearrangements driven by stress adaptation in select density windows, and the typical features of diffusivity (minima $D_{\min}$ at $\simeq 2.1\,\mathrm{g/cm^3}$ and maxima $D_{\max}$ at $3.2\ \mathrm{g/cm^3}$) can be related to the boundaries of the RW. In light of these correlations, we now interpret the location of $D_{\min}$ as the boundary for the onset of a rigid but stress-free network-forming liquid, whereas the location of $D_{\max}$ is related to the upper boundary of the IP. However, the connection with $D_{\max}$ is less clear given that diffusivity maximizes at $\rho \simeq 3.2\,\mathrm{cm^3/g}$, whereas the upper boundary of the RW is located at approximately $3.0\,\mathrm{cm^3/g}$. It should be remembered that the diffusivities are calculated along isotherms, whereas the area A^{ρ} is a global measure of enthalpic changes with temperature. Furthermore, the temperature locus of $D_{\max}$ itself is a decreasing function [103,104] of ρ, and in previous studies it has been emphasized that transport properties are more sensitive to the rigid-to-flexible transition (the lower boundary of the RW) compared to the stressed-to-rigid transition [107], exemplified by the behavior of the floppy mode density with ρ (Fig. 7). This simply reveals that local deformation modes are mostly present in the flexible phase and typical of the low-frequency limit of $g(\omega)$, and they facilitate transport. Once the system becomes rigid, the diffusivity is strongly affected. The other global trends in diffusivity also now become clear. At a low density, the flexible network structure stiffens, and diffusivity decreases with the increase in density until it reaches the RW. The adaptive nature of the system then enhances transport and atomic motion, which induces an increase in diffusivity, promoted by the absence of stress (no redundant bonds/constraints), prior to an important decrease once the system has become stressed rigid and the network is locked by an important bond density that reduces substantially the possibility for diffusion.

An inspection of the density behavior of the sodium diffusivity D_{Na} [Fig. 9(a)] also indicates that this transport coefficient is sensitive to the elastic nature of the network. At a low density ($\rho < 2.1\ \mathrm{g/cm^3}$), D_{Na} displays a nearly constant behavior at a value $D_{\mathrm{Na}} \simeq 12.5 \times 10^{-5}\,\mathrm{cm^2 \cdot s^{-1}}$. However, at the flexible boundary of the RW ($\rho = 2.1\ \mathrm{g/cm^3}$), an obvious change in régime is obtained and D_{Na} decreases substantially upon further densification. In solid electrolytes, the carrier (here Na) mobility μ is directly related to the ion diffusivity via $\mu = D/k_BT$ so that an important mobility change should be expected at the low-density boundary of the RW. The present conclusion is supported by an experimental study and a phenomenological model of the rigidity-conductivty relationship [38,107] in a typical solid electrolyte (AgI-$AgPO_3$). It has been shown, indeed, that a steplike jump in ionic conductivity occurs in glasses becoming isostatically rigid, whereas fast-ion conduction has been found to be largely driven by changes in carrier mobility induced by an elastic softening of network structure, i.e., at a threshold connectivity that can, here, be identified with the lower boundary of the RW at $\rho = 2.1\ \mathrm{g/cm^3}$.

V. CONCLUSION

Glasses inside RWs display anomalous relaxation kinetics that lead to spectacular properties such as weak aging phenomena, fragility minima of the melts, the absence of

internal stress, anomalous mechanical properties, and an enhanced thermal stability. These findings actually have very general grounds because links between the RW and protein folding [108], high-temperature superconductors [109], and computational phase transitions [110] have been stressed. Such deep analogies simply underscore the ability of a complex network to rearrange by adapting internal thermodynamic variables under applied constraints, stress, or conditions. Understanding the IP is therefore of broad interest, as it appears to be a generic feature of disordered networks.

Using MD simulations and topological constraint counting, we have presented a numerical signature of reversible glass transitions, i.e., glass transitions which exhibit a deep minimum in the hysteresis area upon cooling and heating the system. We have, furthermore, shown that this RW is a direct consequence of constraint adaptation in the supercooled liquid. With increasing density, oxygen and silicon coordination increase and lead to a growth of the number of stretching interactions. In order to release part of this increasing stress, angles must soften and must experience larger bond-angle excursions, implying a reduction of corresponding bending interactions/constraints. The increase in stress is also evidenced by the vibrational analysis, which shows that low-frequency modes ($\omega < 10$ meV) in the VDOS associated with the network-forming species (Si, O) progressively disappear as the density is increased.

It is quite remarkable to realize that the present results have a one-to-one correspondence with calorimetric experiments (Fig. 8), and that the behavior of the hysteresis area resulting from the heating/cooling cycles can be directly linked to network adaptation during the glass transition and the dynamics of the system. The thermal (Figs. 1 and 2) and the constraint (Fig. 5) results indicate, indeed, that there exists an obvious correlation between the adaptation of the BO angular constraints via the minimization of the function $q(T,\rho)$, the minimum found in the energy $E^*(T)$, and the area of the cooling/heating cycle. Without stress (present at high densities), which induces bond relaxation, and without floppy modes (present at low densities; Fig. 6), which lead to low-energy relaxation phenomena, an adaptive isostatic system has a significantly different relaxation régime that leads to a minimum in the enthalpic overshoot and the hysteresis appearing in glass transition cycles.

The particular behavior of the system in this pressure window leads to a cascade of other anomalies in structural and dynamic properties in both the liquid and the glassy phase, and obvious correlations emerge when the typical density ranges are compared. Structural anomalies indeed occur in the glassy phase and lead to a maximum in typical correlation lengths and coherence length as revealed from the nonmonotonic evolution with density of the position k_{FSDP} and the width Δk_{FSDP} of the first sharp diffraction peak (FSDP) of partial structure factors [78]. This also suggests that there are structural signatures for the IP, as also demonstrated recently in a numerical study of the archetypal system As-Se [79].

Finally, the present work shows that the theoretical description of RWs now becomes much closer to experiments, given the obvious analogy of the cooling/heating cycle with the upscan/downscan performed in mDSC, which allows accessing a nonreversing enthalpy. However, MD simulations permit access to the evolution of a variety of atomic-scale quantities, and a certain number of other numerical anomalies have been detected in structural, constraint, and dynamic properties when followed as a function of the system density. Our results suggests, indeed, that the anomalous properties that are typical of IPs can now be characterized from MD simulations in detail, and not just from simple-minded models, while also providing strong connections with other (dynamic) observables. This opens the possibility of investigating more complex glasses as a function of the composition, or pressure, or both, as recently reported [30]. In this respect, it clearly marks a step forward in the applicability of rigidity theory and the theoretical description of RWs in real materials as exemplified by the recent study on isostatic cement [30].

ACKNOWLEDGMENTS

The authors thank P. Boolchand, S. Boshle, K. Gunasekera, M. Malki, J.C. Phillips, M. Salanne, and S. Chakraborty for stimulating discussions. Daniel Skoncz-Traintz is acknowledged for technical advice. Support from Agence Nationale de la Recherche (ANR; Grant Nos. 09-BLAN-0109-01 and 11-BS08-0012) is gratefully acknowledged. M.M. acknowledges support from the French-American Fulbright Commission. GENCI (Grand Equipement National de Calcul Intensif) is acknowledged for supercomputing access.

[1] Edited by M. F. Thorpe and P. M. Duxbury, *Rigidity Theory and Applications*, (Kluwer Academic, Plenum, New York, 1999).
[2] Edited by M. Micoulaut and M. Popescu, *Rigidity and Boolchand Intermediate Phases in Nanomaterials* (INOE, Bucarest, 2009).
[3] Edited by M. F. Thorpe and J. C. Phillips, *Phase Transitions and Self-organization in Electronic and Molecular Networks*, (Kluwer Academic, Plenum, New York, 2001).
[4] J. C. Phillips, J. Non-Cryst. Solids **34**, 153 (1979).
[5] M. F. Thorpe, J. Non-Cryst. Solids **57**, 355 (1983).
[6] W. A. Kamitakahara, R. L. Cappelletti, P. Boolchand, B. Halfpap, F. Gompf, D. A. Neumann, and H. Mutka, Phys. Rev. B **44**, 94 (1991).
[7] K. Trachenko and M. T. Dove, Phys. Rev. B **67**, 212203 (2003).
[8] M. Micoulaut, A. Kachmar, M. Bauchy, S. Le Roux, C. Massobrio, and M. Boero, Phys. Rev. B **88**, 054203 (2013).
[9] H. He and M. F. Thorpe, Phys. Rev. Lett. **54**, 2107 (1985).
[10] M. F. Thorpe, J. Non-Cryst. Solids **76**, 109 (1985).
[11] X. Feng, W. J. Bresser, and P. Boolchand, Phys. Rev. Lett. **78**, 4422 (1997).
[12] M. Tatsumisago, B. L. Halfpap, J. L. Green, S. M. Lindsay, and C. A. Angell, Phys. Rev. Lett. **64**, 1549 (1990).
[13] A. N. Sreeram, A. K. Varshneya, and D. R. Swiler, J. Non-Cryst. Solids **128**, 294 (1991).
[14] P. Boolchand, W. J. Bresser, M. Zhang, Y. Wu, J. Wells, and R. N. Enzweiler, J. Non-Cryst. Solids **182**, 143 (1995).

[15] S. Asokan, M. V. N. Prasad, G. Parthasarathy, and E. S. R. Gopal, Phys. Rev. Lett. **62**, 808 (1989).
[16] R. A. Böhmer and C. A. Angell, Phys. Rev. B **45**, 10091 (1992).
[17] A. Srinivasan and K. N. Madhusoodanan, Solid State Commun. **83**, 163 (1992).
[18] M. Nakamura, O. Matsuda, and K. Murase, Phys. Rev. B **57**, 10228 (1998).
[19] U. Senapati and A. K. Varshneya, J. Non-Cryst. Solids **185**, 289 (1995).
[20] J.-P. Guin, T. Rouxel, J.-C. Sangleboeuf, I. Melscoët, and J. Lucas, J. Am. Ceram. Soc. **85**, 1545 (2002).
[21] M. Zhang and P. Boolchand, Science **266**, 1355 (1994).
[22] P. Boolchand and M. F. Thorpe, Phys. Rev. B **50**, 10366 (1994).
[23] F. Wang, P. Boolchand, K. A. Jackson, M. Micoulaut, J. Phys.: Condens. Matter **19**, 226201 (2007).
[24] P. K. Gupta and J. C. Mauro, J. Chem. Phys. **130**, 094503 (2009).
[25] J. C. Mauro, P. K. Gupta, and R. J. Loucks, J. Chem. Phys. **130**, 234503 (2009).
[26] M. Smedskjaer, J. C. Mauro, R. E. Youngman, C. L. Hogue, M. Potuzak, and Y. Yue, J. Phys. Chem. B **115**, 12930 (2011).
[27] J. C. Mauro, R. J. Loucks, and P. K. Gupta, J. Phys. Chem. A **111**, 7957 (2007).
[28] M. M. Smedskjaer, J. C. Mauro, and Y. Yue, Phys. Rev. Lett. **105**, 115503 (2010).
[29] B. P. Rodrigues and L. Wondraczek, J. Chem. Phys. **138**, 244507 (2013).
[30] M. Bauchy, M. J. A. Qomi, C. Bichara, F. J. Ulm, and R. J.-M. Pellenq, Phys. Rev. Lett. **114**, 125502 (2015).
[31] S. King *et al.*, J. Non-Cryst. Solids **379**, 67 (2013).
[32] D. Selvenathan, W. Bresser, and P. Boolchand, Solid State Commun. **111**, 619 (1999).
[33] D. Selvenathan, W. J. Bresser, and P. Boolchand, Phys. Rev. B **61**, 15061 (2000).
[34] F. Wang, S. Mamedov, P. Boolchand, B. Goodman, and M. Chandrasekhar, Phys. Rev. B **71**, 174201 (2005).
[35] S. Chakravarty, D. G. Georgiev, P. Boolchand, and M. Micoulaut, J. Phys.: Condens. Mater. **17**, L1 (2005).
[36] P. Chen, P. Boolchand, and D. G. Georgeiv, J. Phys.: Condens. Matter **22**, 065104 (2010).
[37] M. Micoulaut and M. Malki, Phys. Rev. Lett. **105**, 235504 (2010).
[38] D. I. Novita, P. Boolchand, M. Malki, and M. Micoulaut, Phys. Rev. Lett. **98**, 195501 (2007).
[39] S. Chakraborty, P. Boolchand, M. Malki, and M. Micoulaut, J. Chem. Phys. **140**, 014503 (2014).
[40] B. Wunderlich, J. Therm. Anal. **48**, 207 (1997).
[41] S. Bhosle, K. Gunasekera, P. Boolchand, and M. Micoulaut, Int. J. Appl. Glass Sci. **3**, 205 (2012).
[42] S. Bhosle, K. Gunasekera, P. Boolchand, and M. Micoulaut, Int. J. Appl. Glass Sci. **3**, 189 (2012).
[43] K. Gunasekara, S. Bhosle, P. Boolchand, and M. Micoulaut, J. Chem. Phys. **139**, 164511 (2013).
[44] S. Ravindren, K. Gunasekera, Z. Tucker, A. Diebold, P. Boolchand, and M. Micoulaut, J. Chem. Phys. **140**, 134501 (2014).
[45] R. Bagheria, K. Gunasekera, P. Boolchand, and M. Micoulaut, Phys. Status Solidi **251**, 1322 (2014).
[46] D. I. Novita and P. Boolchand, Phys. Rev. B **76**, 184205 (2007).
[47] M. F. Thorpe, D. J. Jacobs, M. V. Chubynsky, and J. C. Phillips, J. Non-Cryst. Solids **266-269**, 859 (2000).
[48] M. Micoulaut and J. C. Phillips, Phys. Rev. B **67**, 104204 (2003).
[49] J. Barré, A. R. Bishop, T. Lookman, and A. Saxena, Phys. Rev. Lett. **94**, 208701 (2005).
[50] A. N. Cormack, J. Du, and T. R. Zeitler, Phys. Chem. Chem. Phys. **4**, 3193 (2002).
[51] M. Bauchy, B. Guillot, M. Micoulaut, and N. Sator, Chem. Geol. **346**, 47 (2013).
[52] J. Du and A. N. Cormack, J. Non-Cryst. Solids **349**, 66 (2004).
[53] G. J. Kramer, A. J. M. de Man, and R. A. van Santen, J. Am. Chem. Soc. **113**, 6435 (1991).
[54] V. Kahlenberg, Chimia **64**, 716 (2010).
[55] P. G. Debenedetti and F. H. Stillinger, Nature **410**, 259 (2001).
[56] B. O. Mysen and P. Richet, *Silicate Glasses and Melts: Properties and Structure* (Elsevier, Amsterdam, 2005).
[57] G. S. Henderson, Can. Mineral. **43**, 1921 (2005).
[58] M. Micoulaut, Am. Mineral. **93**, 1732 (2008).
[59] O. Williams and R. Jeanloz, Science **239**, 902 (1988).
[60] Y. Guissani and B. Guillot, J. Chem. Phys. **104**, 7633 (1996).
[61] K. Trachenko and M. T. Dove, J. Phys.: Condens. Matter **14**, 1143 (2002).
[62] M. Bauchy and M. Micoulaut, J. Non-Cryst. Solids **357**, 2530 (2011).
[63] N. Zotov, I. Ebbsjö, D. Timpel, and H. Keppler, Phys. Rev. B **60**, 6383 (1999).
[64] B. Champagnon, L. Wondraczek, and T. Deschamps, J. Non-Cryst. Solids **355**, 712 (2009).
[65] S. N. Taraskin and S. R. Elliott, Phys. Rev. B **56**, 8605 (1997).
[66] Y. Cai and M. F. Thorpe, Phys. Rev. B **40**, 10535 (1989).
[67] K. Trachenko, M. T. Dove, V. V. Brazhkin, and F. S. El'kin, Phys. Rev. Lett. **93**, 135502 (2004).
[68] M. D. Newton, M. O'Keeffe, and G. V. Gibbs, Phys. Chem. Minerals **6**, 305 (1980).
[69] G. G. Naumis, Phys. Rev. B **73**, 172202 (2006).
[70] O. Laurent, B. Mantisi, and M. Micoulaut, J. Phys. Chem. B **118**, 12750 (2014).
[71] M. Micoulaut, J.-Y. Raty, C. Otjacques, and C. Bichara, Phys. Rev. B **81**, 174206 (2010).
[72] M. Bauchy, M. J. A. Qomi, C. Bichara, F.-J. Ulm, and R. J.-M. Pellenq, J. Phys. Chem. C **118**, 12485 (2014).
[73] M. Bauchy, J. Chem. Phys. **137**, 044510 (2012).
[74] M. V. Chubynsky, M. A. Briére, and N. Mousseau, Phys. Rev. E **74**, 016116 (2006).
[75] C. F. Moukarzel, Phys. Rev. E **88**, 062121 (2013).
[76] L. Yan and M. Wyart, Phys. Rev. Lett. **113**, 215504 (2014).
[77] F. Inam, G. Chen, D. N. Tafen, and D. Drabold, Phys. Status Solidi B **246**, 1849 (2009).
[78] M. Micoulaut and M. Bauchy, Phys. Status Solidi B **250**, 976 (2013).
[79] M. Bauchy, M. Micoulaut, M. Boero, and C. Massobrio, Phys. Rev. Lett. **110**, 165501 (2013).
[80] M. T. M. Shatnawi, C. L. Farrow, P. Chen, P. Boolchand, A. Sartbaeva, M. F. Thorpe, and S. J. L. Billinge, Phys. Rev. B **77**, 094134 (2008).
[81] M. Micoulaut, J. Phys.: Condens. Matter **22**, 285101 (2010).
[82] S. Chakraborty and P. Boolchand, J. Phys. Chem. B **118**, 2249 (2014).

[83] D. G. Georgiev, P. Boolchand, and M. Micoulaut, Phys. Rev. B **62**, R9228(R) (2000).
[84] P. Chen, C. Holbrook, P. Boolchand, D. G. Georgiev, K. A. Jackson, and M. Micoulaut, Phys. Rev. B **78**, 224208 (2008).
[85] D. G. Georgiev, P. Boolchand, H. Eckert, M. Micoulaut, and K. Jackson, Europhys. Lett. **62**, 49 (2003).
[86] P. Boolchand, P. Chen, and U. Vempati, J. Non-Cryst. Solids **355**, 1773 (2009).
[87] Y. Wang, J. Wells, D. G. Georgiev, P. Boolchand, K. A. Jackson, and M. Micoulaut, Phys. Rev. Lett. **87**, 185503 (2001).
[88] T. Qu, D. G. Georgiev, P. Boolchand, and M. Micoulaut, Mater. Res. Soc. Proc. **754**, 111 (2003).
[89] T. Qu and P. Boolchand, Philos. Mag. **85**, 875 (2005).
[90] U. Vempati and P. Boolchand, J. Phys.: Condens. Matter **16**, S5121 (2004).
[91] K. Gunasekera, P. Boolchand, and M. Micoulaut, J. Phys. Chem. B **117**, 10027 (2013).
[92] K. Gunasekera, P. Boolchand, and M. Micoulaut, J. Appl. Phys. **115**, 164905 (2014).
[93] C. Das, M. R. S. N. Kiran, U. Ramamurty, and S. Asokan, Solid State Commun. **152**, 2181 (2012).
[94] G. S. Varma, C. Das, S. Asoka,, Solid State Commun. **177**, 108 (2014).
[95] P. Boolchand (unpublished).
[96] R. Rompicharla, D. I. Novita, P. Chen, P. Boolchand, M. Micoulaut, and W. Huff, J. Phys.: Condens. Matter **20**, 202101 (2008).
[97] S. Vignarooban, P. Boolchand, M. Malki, and M. Micoulaut, Europhys. Lett. **108**, 56001 (2014).
[98] C. Bourgel, M. Micoulaut, M. Malki, and P. Simon, Phys. Rev. B **79**, 024201 (2009).
[99] M. Bauchy and M. Micoulaut (unpublished).
[100] G. E. Henderson and M. E. Fleet, J. Non-Cryst. Solids **134**, 259 (1991).
[101] M. Bauchy and M. Micoulaut, Phys. Rev. Lett. **110**, 095501 (2013).
[102] M. Bauchy and M. Micoulaut, Phys. Rev. B **83**, 184118 (2011).
[103] M. S. Shell, P. G. Debenedetti, and A. Z. Panagiotopoulos, Phys. Rev. E **66**, 011202 (2002).
[104] J. R. Errington and P. G. Debenedetti, Nature **409**, 318 (2001).
[105] F. Pacaud and M. Micoulaut, J. Chem. Phys. **143**, 064502 (2015).
[106] P. L. Chau and A. J. Hardwick, Mol. Phys. **93**, 511 (1998).
[107] M. Micoulaut, M. Malki, D. I. Novita, and P. Boolchand, Phys. Rev. B **80**, 184205 (2009).
[108] D. J. Jacobs, A. J. Rader, L. A. Kuhn, and M. F. Thorpe, Proteins **44**, 150 (2001).
[109] J. C. Phillips, Phys. Rev. Lett. **88**, 216401 (2002).
[110] R. Monasson, R. Zecchina, S. Kirkpatrick, B. Selman, and L. Troyansky, Nature **400**, 133 (1999).